remote sensing

MDPI

Article

Scintillations in Southern Europe During the Geomagnetic Storm of June 2015

Anna Morozova [1,2,*], Luca Spogli [3], Teresa Barata [1], Rayan Imam [3], Emanuele Pica [3], Juan Andrés Cahuasquí [4], Mohammed Mainul Hoque [4], Norbert Jakowski [4] and Daniela Estaço [5,†]

[1] Instituto de Astrofísica e Ciências do Espaço, University of Coimbra, 3004-531 Coimbra, Portugal; teresabarata@dct.uc.pt
[2] Department of Physics, Faculty of Sciences and Technologies, University of Coimbra, 3004-531 Coimbra, Portugal
[3] Istituto Nazionale di Geofisica e Vulcanologia, 00143 Rome, Italy; luca.spogli@ingv.it (L.S.); rayan.imam@ingv.it (R.I.); emanuele.pica@ingv.it (E.P.)
[4] Institute for Solar-Terrestrial Physics, German Aerospace Center DLR, 17235 Neustrelitz, Germany; andres.cahuasqui@dlr.de (J.A.C.); mainul.hoque@dlr.de (M.M.H.); norbert.jakowski@dlr.de (N.J.)
[5] Departament of Physics, University of Aveiro, 3810-193 Aveiro, Portugal; danielaestaco@ua.pt
* Correspondence: anna.morozova@uc.pt
† Current address: Department of Physics, Instituto Superior Técnico, University of Lisbon, 1049-001 Lisbon, Portugal.

Abstract: The sensitivity of Global Navigation Satellite System (GNSS) receivers to ionospheric disturbances and their constant growth are nowadays resulting in an increased concern of GNSS users about the impacts of ionospheric disturbances at mid-latitudes. The geomagnetic storm of June 2015 is an example of a rare phenomenon of a spill-over of equatorial plasma bubbles well north from their habitual. We study the occurrence of small- and medium-scale irregularities in the North Atlantic Eastern Mediterranean mid- and low-latitudinal zone by analysing the amplitude of the scintillation index S4 and rate of total electron content index (ROTI) measurements during this storm. In addition, large-scale perturbations of the ionospheric electron density were studied using ground and space-borne instruments, thus characterising a complex perturbation behaviour over the region mentioned above. The involvement of large-scale structures is emphasised by the usage of innovative approaches such as the ground-based gradient ionosphere index (GIX) and electron density and total electron content gradients derived from Swarm satellite data. The multi-source data allow us to characterise the impact of irregularities of different scales to better understand the ionospheric dynamics and stress the importance of proper monitoring of the ionosphere in the studied region.

Keywords: scintillations; S4; ROTI; GIX; equatorial plasma bubbles; equatorial plasma bubbles spill-over; mid-latitudinal ionosphere; ionospheric gradients

check for updates

Academic Editors: Veronika Barta, Christina Arras and Jaroslav Urbar

Received: 10 December 2024
Revised: 28 January 2025
Accepted: 29 January 2025
Published: 5 February 2025

Citation: Morozova, A.; Spogli, L.; Barata, T.; Imam, R.; Pica, E.; Cahuasquí, J.A.; Hoque, M.M.; Jakowski, N.; Estaço, D. Scintillations in Southern Europe During the Geomagnetic Storm of June 2015. *Remote Sens.* **2025**, *17*, 535. https://doi.org/10.3390/rs17030535

1. Introduction

The analysis presented here aims to investigate a rare event of a spill-over of equatorial plasma bubbles (EPBs) from low latitudes, triggered by the occurrence of a geomagnetic storm. These spill-over events are gaining more interest as they are one of the main sources of storm-trigger Global Navigation Satellite System (GNSS) disturbances at mid-latitudes. A first assessment of this class of disturbances on the investigated storm has been proposed by [1], who reported on large-scale EPB events covering the Mediterranean sector.

As highlighted by [2], the conditions favouring the spill-over of EPBs at mid-latitudes are mostly due to the occurrence of storm-induced prompt penetration electric fields, PPEFs [3], occurring near the local sunset hours at the geomagnetic equator and that may intensify the EPB seeding process due to pre-reversal enhancement [4]. This has also been nicely illustrated during the recent May 2024 Mother's Day superstorm, during which a meaningful EPB spill-over was recorded over the Mediterranean [5]. The authors of [6] reported a mid-latitude scintillation event over the Southern United States on June 1, 2013, occurring during the main phase of a modest magnetic storm. This suggests that the intensity of the storm is not the primary factor; rather, it is the local time of the occurrence of the PPEF event that triggers the EPB spill-over at mid-latitudes.

The geomagnetic storm of June 2015 and its effects on the ionospheric conditions are well described in previous work: see, for example, [7–9] and references therein for a detailed description of this geomagnetic storm development and ionospheric responses with a focus on the region studied in this work (the West Mediterranean, the Iberian Peninsula and a part of the eastern North Atlantic Ocean between Azores, Canary and Madeira archipelagos and the northwestern African coast, or 0–50°N in latitude and 65°W–65°E in longitude; see also Figure 1).

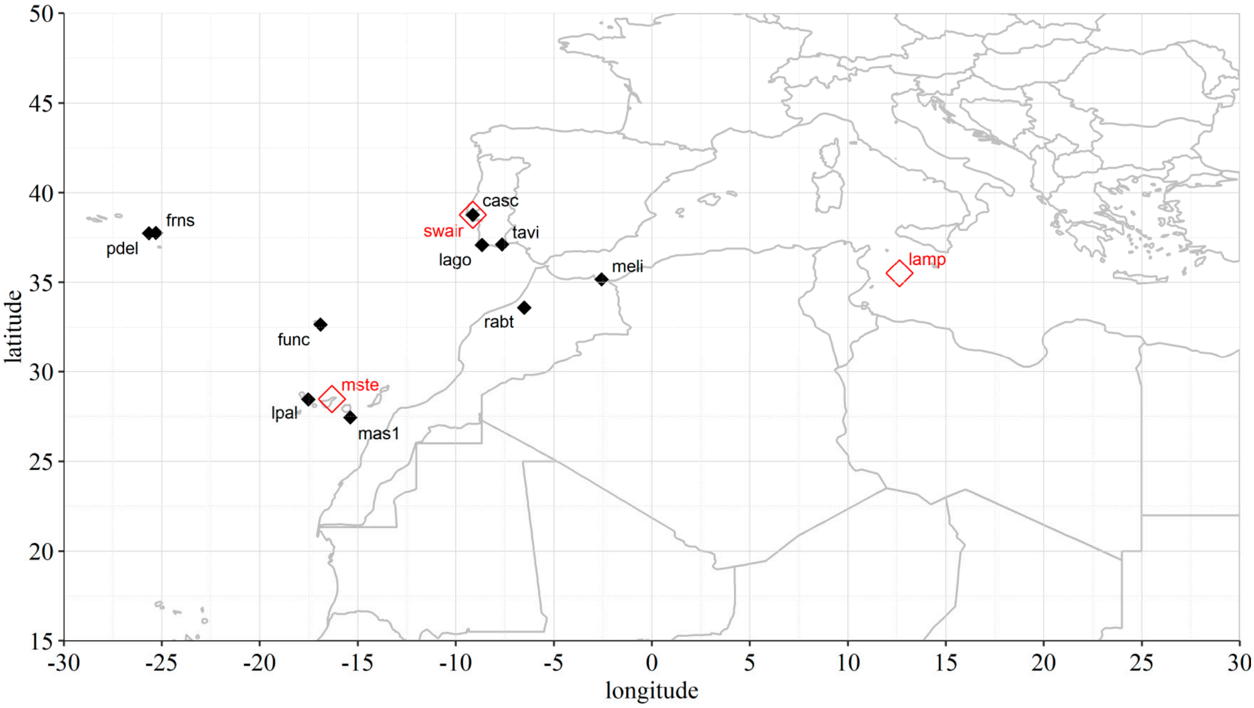

Figure 1. Locations of GNSS receivers used to calculate S4 (red open diamonds) and ROTI (black diamonds) scintillation indices.

In brief, the storm of 22–23 June 2015 was the second-strongest geomagnetic storm of the 24th solar cycle, caused by three consecutive coronal mass ejections [10,11]. The response of the ionosphere during its initial phase was asymmetric concerning the hemispheres, mainly due to seasonal effects, with a negative phase of the storm observed in most of the northern hemisphere and a positive phase in the southern hemisphere and western longitudes of the northern hemisphere, over the North Atlantic Ocean—the area of our study. The total electron content (TEC) variations were obtained from Portuguese GNSS receivers located in Lisbon (Iberian Peninsula), S. Miguel Island (Azores) and Madeira Island [7,9] and consisted of a strong positive ionospheric storm that started in the late afternoon of 22 June (ΔTEC ~+20 TECu) and a strong negative ionospheric storm (ΔTEC ~−20 TECu) on the following day, 23 June 2015. A secondary Dst drop on 25 June 2015 caused another positive–negative ionospheric storm observed on 25–26 June [7,9], but the secondary event was not accompanied by scintillations and, therefore, is not analysed in this work.

The storm of 22 June 2015 was associated with PPEFs [12], and as was mentioned before, these conditions may be favourable for both the development of EPBs during the storm time and their spill-over to the middle latitudes. Such a rare phenomenon as an EPB spill-over was observed twice during this storm: first in the Euro–African longitudinal sector between 20 h UTC on 22 June and 2 h UTC on 23 June, and later, between 4 h UTC and 7 h UTC on 23 June, in the American longitudinal sector [12]. The EPB spill-over resulted in strong scintillations of the GNSS signal in the middle latitudes, as, for example, is reported in [1,8]. In particular, the quality of the relative positioning, especially the single frequency relative positioning [8], for the area of the Iberian Peninsula decreased drastically between 18–19 h UTC on 22 June and 6–8 h UTC on 23 June. Those high positioning errors were found to be coincident with periods of high spatial TEC gradient of the medium to large scales, as reported by [8] using the gradient ionosphere index (GIX).

Previously, the scintillation event of 22–23 June 2015, as related to the EPB spill-over, was studied using the rate of TEC index (ROTI) [13], obtained both from the ground-based GNSS receivers and from space-borne instruments [1,11,12,14] as well as data on spatial and temporal TEC gradients [8].

In this work, we present, for the first time, an analysis of this event using the amplitude scintillation index S4 [15,16] obtained at three locations in the Mediterranean—North Atlantic area (15°N–50°N, 25°W–30°E). The S4 data are complemented with ROTI obtained from ground-based instruments of two kinds: geodetic receivers and ionospheric scintillation monitoring receivers (ISMRs) [17,18]. The geodetic receivers can provide total electron content (TEC) and the index based on its rate of change (ROTI), while the scintillation receivers provide the amplitude scintillation index S4. Since the variations in the S4 and ROTI indices may result from ionospheric inhomogeneities of different spatial scales [19], the comparison of the S4 and ROTI data will provide insight into the dynamics of the ionosphere during the studied event. The character of the ionospheric electron density inhomogeneities (size, location, travelling direction) was obtained from the analysis of the slant TEC (sTEC) data and the spatial TEC gradients calculated for the whole studied area using ground-based data sources and the Swarm datasets.

2. Data

2.1. S4 and ROTI Data

The data on the scintillation index variations, the amplitude scintillation index S4 and ROTI are obtained from a set of GNSS receivers.

2.1.1. S4 Data

In the presented analysis, we focus on the S4 index computed at 1-min intervals, able to reveal the impact of small-scale irregularities on the received signal. These have a typical scale size below Fresnel's scale for L-band signals and GNSS observational geometry from the ground, i.e., a scale of a few hundred metres [20].

Data from three receivers were used to analyse S4 variations during the studied event. The original data have a 1-min time resolution and were obtained using GPS satellites only. These receivers are marked as open red diamonds in Figure 1.

Lisbon. The S4 data for Lisbon were obtained by a geodetic Septentrio GNSS receiver with SCINDA software (version of 2013) installed in the area of the Lisbon airport (38.70°N, 9.14°W) between 2014 and 2019. The acquisition and processing of the data are described in detail in [21,22]. The data were validated during the PITHIA NRF TNA project ALERT [23].

Lampedusa. The S4 data for Lampedusa Island (35.52°N, 12.63°E) were obtained from a Novatel GSV4004B ISMR [17], which operated at the Climate Observation Station of the Italian National Agency for New Technologies, Energy and Sustainable Economic Development (ENEA) between June 2011 and November 2018. The receiver owner is the INGV, and the data are available through the eSWua system (eswua.ingv.it, station code: "lam0s") [24]. The data on the slant S4 were used.

The GSV4004B was a single constellation (GPS only) scintillation receiver with multi-frequency capabilities, able to evaluate amplitude scintillation by calculating the S4 index, which is the standard deviation of the received power normalised by its mean value [14]. Specifically, this is derived from the detrended received signal intensity. A high-pass filter is applied to detrend the raw amplitude measurements, as described by [17]. A fixed cutoff frequency of 0.1 Hz at 3 dB is used for both phase and amplitude filtering.

Tenerife. The S4 data for the Canary Islands are from a Trimble Zephyr Geodetic II receiver installed at Tenerife Island (28.48°N, 16.32°W) and operated by Universidad de La Laguna and the German Aerospace Center (DLR).

2.1.2. RINEX-Based ROTI Data

RINEX files from the GNSS receivers installed in the studied area (black diamonds in Figure 1) were used to calculate the ROTI index. Some of them belong to the Portuguese network of geodetic GNSS receivers RENEP (Rede Nacional de Estações Permanentes GNSS, https://renep.dgterritorio.gov.pt/, accessed on 12 December 2024)—pdel, frns, func, casc, lago, and tavi. Other receivers are accessible through the FTP repository of the International GNSS Service (IGS: https://igs.org/, accessed on 12 December 2024).

2.2. Japanese ROTI and TEC Maps

To study TEC and ROTI variations, we also used products developed in the frame of the Dense Regional and Worldwide International GNSS-TEC observation (DRAWING-TEC) project led by the Institute for Space–Earth Environmental Research (ISEE, https://aer-nc-web.nict.go.jp/GPS/DRAWING-TEC/, accessed on 12 December 2024). The two-dimensional maps we used (the absolute TEC and ROTI) had a grid size of 0.5 × 0.5° and a 5-min time resolution, which we averaged to have a 15-min time resolution. The maps were originally built using RINEX files obtained from more than 9300 GNSS receivers all over the world (as of January 2020).

2.3. Swarm Ionospheric Plasma Bubble Index

The ionospheric bubble index (a Swarm product SW_IBIxTMS_2F, https://swarmhandbook.earth.esa.int/catalogue/sw_ibixtms_2f, accessed on 12 December 2024) was used to confirm EPB appearance in the studied area on 22–23 June 2015. The product provided flagged data related to the plasma bubble index.

In total, six events of EPB detection were found for the studied region and the studied time interval. However, three of those EPB detections were too far east (at 18:30, 20:00 and 21:30 UTC on 22 June), and one EPB detection was too far west (23 June 02:00 UTC) from the studied region. Thus, only two EPB events detected by Swarm were used in this analysis: on 22 June at 23:00 UTC (Swarm A and C, latitudinal range 21–30°N between 4.5° and 6°W in longitude) and on 23 June at 01:00 UTC (Swarm B, latitudinal range 27–40°N and near 3°W in longitude).

2.4. GIX, NeGIX and TEGIX Indices

This investigation also integrates a set of indices developed with the aim of monitoring and characterising the perturbation degree of the ionosphere at mid-scales, in the order of a few 10s and up to some 200 km.

The gradient ionosphere index (GIX) [25] benefits from ground-based GNSS observations to estimate spatial gradients in the TEC domain. In this study, GIX values are computed using link-related absolute/calibrated slant TEC instead of VTEC maps to minimise ionosphere mapping errors. Ground-based data from the IGS network are used to create half-hourly (with 1 × 1° latitude and longitude resolution) maps of the 95-percentile metric of the GIX from 20:30 UTC on 22 June until 02:00 UTC on 23 June.

Additionally, using Swarm satellites A and C, two data products have been recently developed to explore ionospheric perturbations at mid-scales, between 30 and 200 km [26]. The electron density gradient index (NeGIX, SW_NIX_TMS_2F) uses in situ Langmuir Probe data to estimate plasma density gradients at the height of the spacecraft, whereas the total electron content gradient index (TEGIX, SW_TIX_TMS_2F) uses level 2 GNSS data to compute TEC gradients in the topside ionosphere. Both products have a resolution of 0.5° in latitude, or about 8 s, along the track of the satellites. The near-parallel orbits of Swarm A and C that reach a separation of ca. 180 km at the equator (in June 2015) and the combination of measurements within this resolution permits to compute gradient vectors not only meridionally along the path of the satellites but also in the zonal (west–east) direction.

On 22–23 June 2015, Swarm satellites A and C observed the stronger phase of this geomagnetic storm above the Iberian Peninsula during their descending orbits, with an equatorial pass at 23 h local time. Over the investigated region 65°W–65°E and 0–50°N, five passes of the Swarm pair were recorded from the evening of 22 June to the early hours of 23 June at 19:58 UTC, 21:32 UTC, 23:06 UTC, 00:40 UTC, and 02:14 UTC. Respectively, they flew along longitudes 41.5°E, 18°E, 5.5°W, 29°W, and 52.5°W. A pass over the 50-degree latitudinal section lasts around 13 min.

3. Methods

3.1. Multipath Detection

The multipath contamination of the S4 series was studied, and the data for all three stations were cleaned using the sidereal multipath mask method.

This method relies on the repeated satellite visit every 23 h and 56 min (i.e., sidereal day) of GPS satellites to detect the multipath sources (buildings, etc.) causing scintillation-like S4 index inflations [27,28]. Assuming the multipath sources are static for many days, when S4 is high for several days at the same sidereal time, that indicates a non-scintillation-related signal disturbance. Scintillation is random by nature, and we do not expect to see the same S4 for consecutive days at the same exact sidereal time. The average 7-day sidereal S4 (24 h minus 4 min for GPS) is evaluated per PRN (pseudorandom noise codes unique to each GNSS satellite). The maximal S4 value in these 7 days was excluded, i.e., considered an outlier, to avoid inflating the average sidereal S4 with the S4 resulting from scintillation. We use this average sidereal S4 as a mask to discard multipath contaminated data from the analysis.

Figure 2a shows the Lisbon S4 data plotted as a function of the ionosphere piercing points (IPPs) date and time. The diagonal lines in Figure 2a correspond to individual satellites and result from the difference in the day length for a receiver (24 h) and revisiting time for each of the satellites (23 h 56 min). These diagonal lines show the multipath contamination. Also, a clear scintillation event is visible as coloured vertical stripes at the end of 22 June and during the early hours of 23 June. The results of the sidereal S4 analysis are presented in Figure 2b. As one can see from the comparison of these plots (similar plots for Tenerife and Lampedusa can be found in the Supplementary Materials, SM, Figures S1 and S2), the sidereal S4 analysis provides a dataset of S4 that is reliably cleared from the multipath effect and keeps the data related to the event.

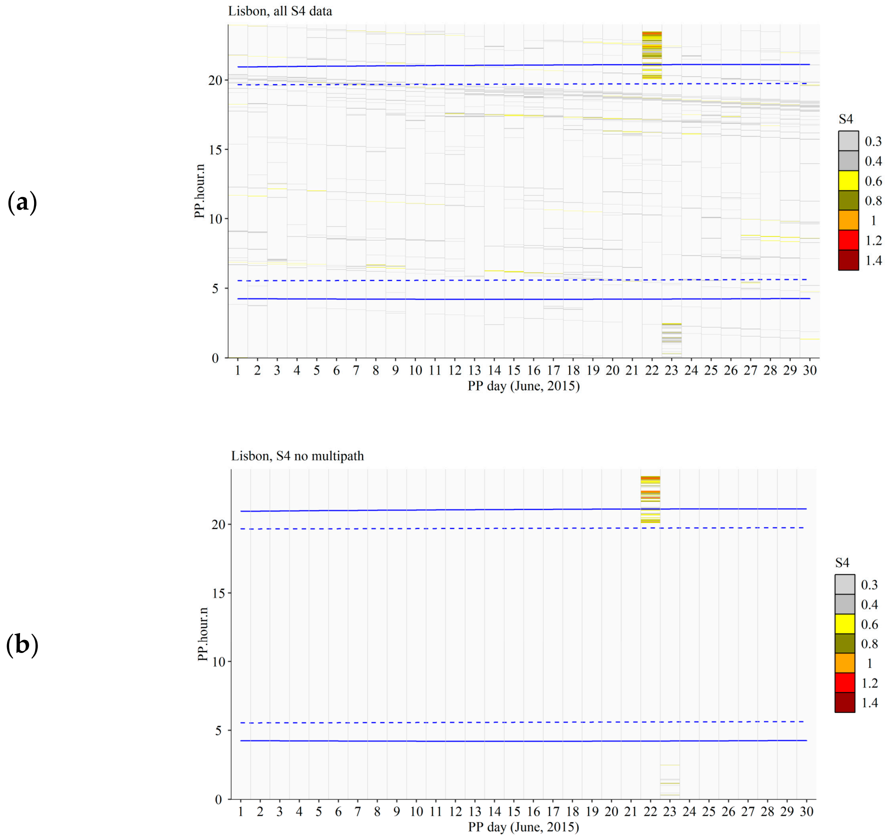

Figure 2. S4 data (colours) for Lisbon for June 2015 as a function of PP hours and days: (**a**) all data, and (**b**) removing multipath contamination using sidereal S4 analysis.

3.2. TEC Gradient Maps

Spatial ionospheric gradients reflect spatial changes in the electron density and can be used to line out local areas with higher/lower electron density compared to the surrounding ionosphere. An analysis of the spatial TEC gradients can be used to detect boundaries of such structures as EPBs.

In this study, we used the approach developed by [29] based on Global Ionospheric Maps (GIMs) to compute spatial gradients. Spatial TEC gradients are calculated as differences between TEC values at adjacent grid points (i,j) (see Figure 3) at the same latitude ($\triangledown$xTEC or $\triangledown x_j$ in Equation (1)) or longitude ($\triangledown$yTEC or $\triangledown$y in Equation (2)), which are then used to determine the absolute gradient ($\triangledown$TEC or $\triangledown$ in Equation (3)):

$$\triangledown x_{i,j} = (\mathrm{TEC}_{i,j} - \mathrm{TEC}_{i-1,j})/\Delta\mathrm{Lon}, \tag{1}$$

$$\triangledown y_{i,j} = (\mathrm{TEC}_{i,j} - \mathrm{TEC}_{i,j-1})/\Delta\mathrm{Lat}, \tag{2}$$

and

$$(\triangledown_{i,j})^2 = (\triangledown x_{i,j})^2 + (\triangledown y_{i,j})^2, \tag{3}$$

where ΔLon and ΔLat are grid steps (in km) along the longitude and latitude, respectively. In this work, the spatial TEC gradients (in mTECu/km) were calculated for the studied region using TEC maps provided by the DRAWING-TEC project for the studied area between 25°W and 30°E and between 15°N and 50°N. The choice of the DRAWING-TEC products instead of GIMs is justified by the low spatial resolution (5° longitude by 2.5° latitude) of the openly available GIMs compared to the DRAWING-TEC products, as well as by significant smoothing of the TEC spatial variations resulting from the fitting of the GNSS data by the spherical harmonics basis functions during the GIMs production. The usage of GNSS-based TEC maps (as the DRAWING-TEC products) allows us to obtain more realistic TEC gradients with high temporal and spatial resolution (compared to GIM-based gradients). On the other hand, the areas of valid TEC observations are constrained by the availability of GNSS receivers and the relative position of GNSS satellites observed by each of these receivers at certain time intervals.

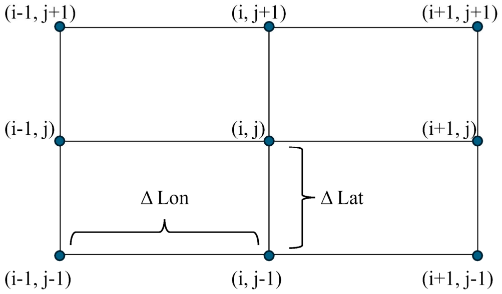

Figure 3. Scheme of the calculation of the spatial TEC gradients using TEC maps (adopted from [29]).

Please note that neither the DRAWING-TEC maps nor the spatial TEC gradients derived from them are used to calculate gradient indices (GIX, NeGIX and TEGIX), as described in Section 4.4.

4. Scintillation Event of 22–23 June 2015

4.1. S4 from Ground-Based Receivers

The analysis of the 22–23 June 2015 scintillation event presented in this work is based on the data from three ground-based GNSS receivers located in the Mediterranean–Atlantic region (marked as open red diamonds in Figure 1) in Lisbon and at Tenerife and Lampedusa islands. The Lisbon and Tenerife receivers are located close to the region(s) where anomalies in TEC and ROTI variations were detected in previous studies [1,12], while the Lampedusa receiver is located well to the east of this region.

Significant S4 time variations during the days of 22–23 June 2015 were observed at these three locations. Scintillations (S4 > 0.5) were observed at all three stations during the night of 22–23 June 2015, starting from around 20 h UTC. However, the strength of the scintillation event depends on the location. The highest S4 values were observed at Tenerife, and the peak of S4 was observed there earlier than at other stations (around 21 h UTC). The time variations in S4 let us identify two periods of scintillations: on 22 June from ~19:30 to ~23:30 UTC (with maxima at ~21:00 and 21:45–22:00 UTC) and on 23 June from around midnight to ~03:00 UTC (maximum at ~01:00 UTC). Scintillations (S4 > 0.5) were observed at Lisbon. However, the amplitude of S4 variations there is smaller than at Tenerife, and the peak of S4 was observed much later (near midnight). Also, at Lisbon, it is possible to identify four periods of increased S4: on 22 June at ~20:00–21:00 UTC, ~21:30–22:30 UTC and, with the largest S4 values, at ~22:45–23:45 UTC, and on 23 June at ~02:00–02:30 UTC with S4 values near or slightly above the scintillation threshold. While scintillations were observed by the Lampedusa receiver, their amplitude was much lower than at the other two stations. This can be explained by the location of this receiver too far to the east from the scintillation sources. Here, there were two periods of high S4 values on 22 June at ~20:00–20:30 UTC and ~21:30–22:40 UTC and two periods with S4 values below the threshold of S4 = 0.5 but still higher than the baseline: on 22 June at ~22:45–23:45 UTC and on 23 June at ~01:30–02:00 UTC. These time variations in S4 can be deduced from Figures 4 and S5 (or can be seen in Figure S3 in the Supplementary Materials).

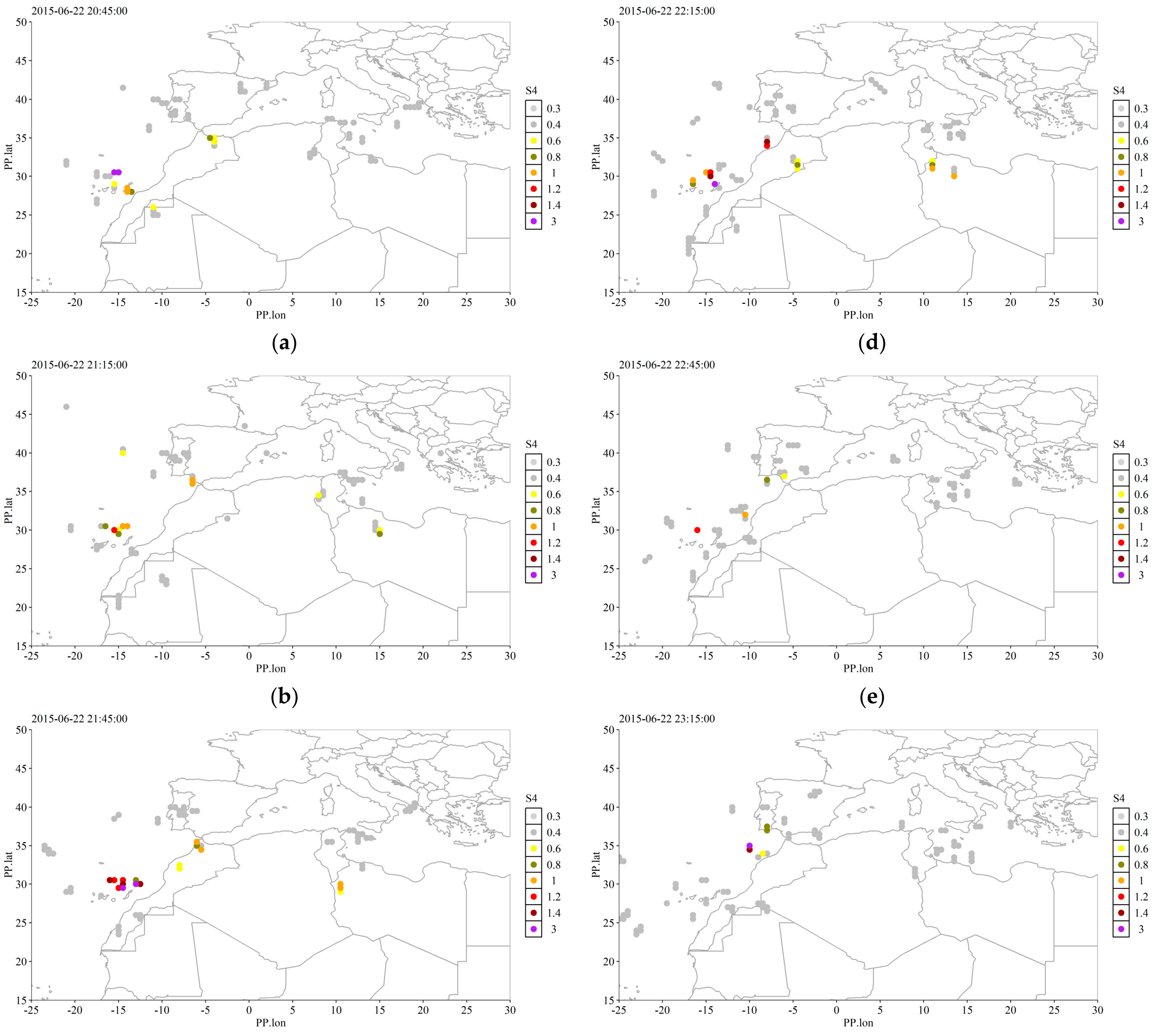

(**a**) (**d**)

(**b**) (**e**)

(**c**) (**f**)

Figure 4. S4 (coloured dots) at IPP coordinates collected for 15 min on 22 June between 20:45 and 23:30 (top to down, left to right, please see the time stamps).

The distributions of the S4 values, depending on the azimuth and elevation of satellites during the days of 22–23 June 2015, depend on the station (can be deduced from Figures 4 and S5 and are shown in Figure S4 in the Supplementary Materials for all three stations). For Lisbon, all affected satellites were located to the south and southeast of the receiver (azimuth between 120° and 195°). Both low (<20°) and high (≥20°) elevation satellites were affected. For Tenerife, most of the high S4 values were observed for the satellites located to the north and northeast (azimuth range 0–105° and 330–360°) from the receiver. Also, S4 > 0.5 values were observed for satellites directly to the south of the receiver (azimuth 180°). All the satellites seen by the Tenerife receiver affected by the scintillations have elevations above 20° (some were at elevations close to 80–90°). Satellites seen by the Lampedusa receiver that were affected by scintillations were in a broad range of azimuth (from ~150° to ~240°) and located in the south and southwest directions from the receiver. Almost all the affected satellites have an elevation <50°.

The analysis of the azimuth–elevation distribution of S4 for all three receivers allows us to assume that the sources of the scintillations observed in the studied region during the night of 22–23 June 2015 were travelling in the area between the Iberian Peninsula and the Canary Islands. This assumption is also confirmed by the maps shown in Figure 4 and in the Supplementary Materials (Animation S1). These maps show S4 values at IPPs (collected at 15-min time intervals starting from the timestamp of a map) on 22 June between 20:45 and 23:30 (Figure 4) and on 23 June between 00:15 and 01:45 (Figure S5). These time intervals are periods of the most intense scintillations (see Figure S3).

The maps show that IPPs for the observations associated with high S4 values are mostly located in a region between the Canary Islands and the Iberian Peninsula, above northwestern Africa and the neighbouring areas of the Atlantic Ocean. Also, weak scintillations are associated with IPPs over Northern Africa (to the south of Lampedusa).

Based on the S4 data analysis, we conclude that the scintillations were caused by sources that passed over Northern and northwestern Africa and further on over the North Atlantic Ocean. The scintillation sources were moving generally in the northwest direction, as is seen in Animation S1 (Supplementary Materials).

4.2. ROTI Indices: Ground-Based Receivers and Maps

To further study the scintillation event of 22–23 June 2015, we analysed the ROTI indices obtained both from the RINEX files of several receivers (black diamonds in Figure 1) and from ROTI maps provided by the DRAWING-TEC project. Figures 5 and S6 show ROTI obtained from ground-based receivers in the studied area binned to the $0.5 \times 0.5°$ grid for the same time intervals as Figures 6 and S5 (see also Supplementary Materials Animation S1).

The ROTI data from the ground-based receivers confirm the finding based on the analysis of S4: the sources of scintillations during the studied time interval were in a wide band between the Canary Islands and the Iberian Peninsula. The strongest scintillations were observed in the late afternoon of 22 June (between 20:30 UTC and 23:30 UTC), followed by a smaller amplitude increase in the scintillations during the first hours of 23 June (between 00:00 UTC and 02:00 UTC). During the scintillation event, the locations of the scintillation sources were slowly moving in the northwest direction.

This conclusion is confirmed by the ROTI. Figures 6 and S7 in SM show the ROTI maps for the same time intervals as in Figures 5 and S6, respectively, (colour scheme) with superimposed ROTI data from the ground-based receivers (coloured open circles) and the Swarm ionospheric plasma bubble index (grey dots along meridians). An animation can be found in the Supplementary Materials (Animation S3).

Since the S4 and ROTI indices can be considered as measures to detect the electron density inhomogeneity on different spatial scales [19]—smaller scales (a few hundred metres) for S4 and medium scales (few kilometres) for the 5-min ROTI from 30 s RINEX at low latitudes—we compared the ROTI and S4 data. Figures 7 and S8 in SM show ROTI maps for the same time intervals as before (colour scheme) with superimposed S4 data from the ground-based receivers (white/black open circles, see figure captions) and the Swarm ionospheric plasma bubble index (grey dots along meridians). An animation can be found in the Supplementary Materials (Animation S4).

The S4 data are available only for three ground-based receivers and are limited to the satellites available during the studied time interval. Thus, the spatial coverage of the S4 data is much sparser than that of the ROTI data. However, high S4 values (black circles) tend to cluster in the regions with higher ROTI values (green to reddish colours). The link between ROTI and S4 is more clearly seen during the night hours of 22 June than during the early hours of 23 June since the amplitudes of both S4 and ROTI variations during the scintillation event were much higher on 22 June.

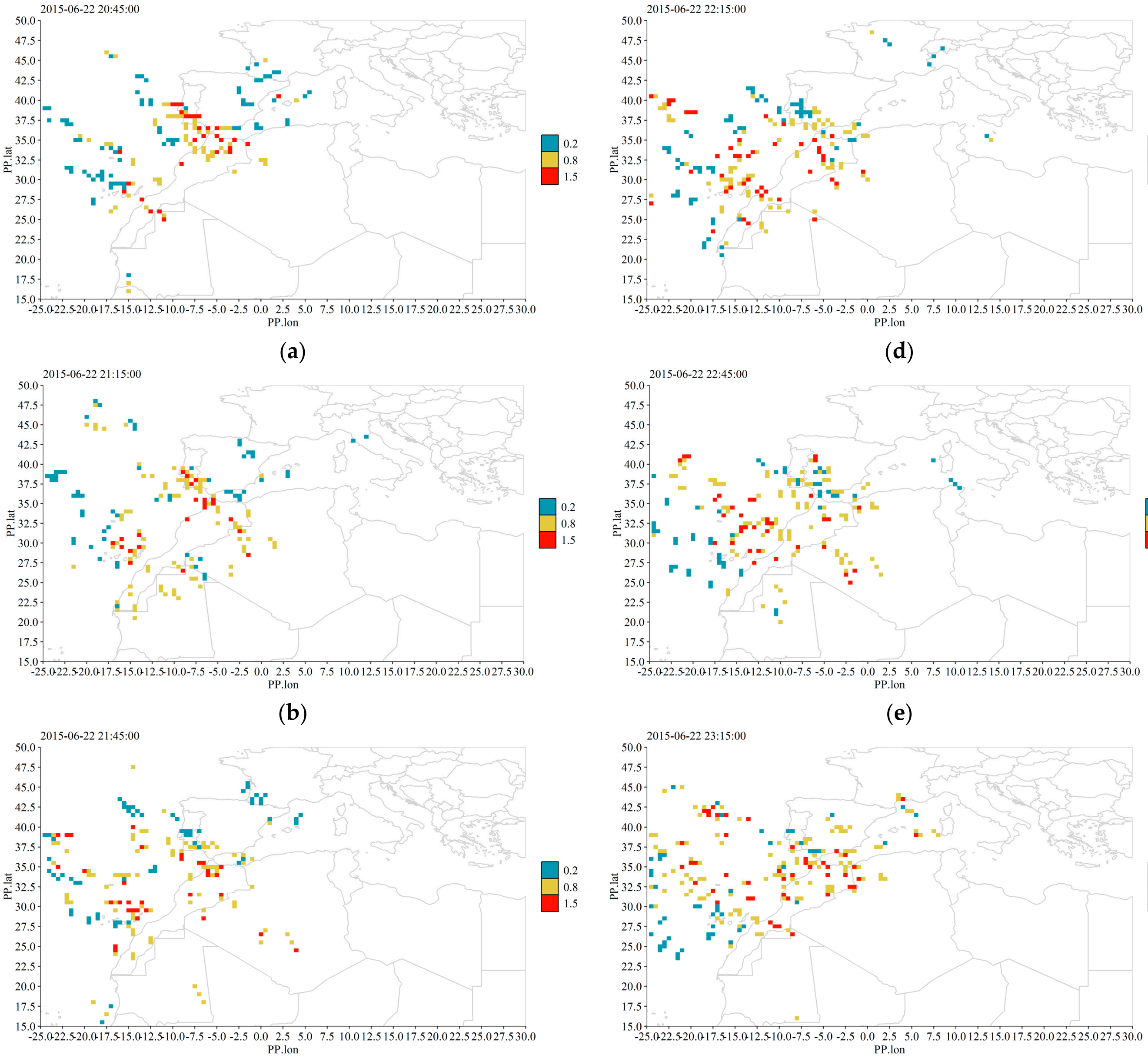

(**a**) (**d**)

(**b**) (**e**)

(**c**) (**f**)

Figure 5. ROTI values from receivers (colour) binned to 0.5 × 0.5° grid collected for 15 min on 22 June between 20:45 and 23:30 (top to down, left to right, please see the time stamps).

The comparison of the S4 and ROTI variations allows us to conclude that the scintillation event of 22–23 June 2015 was caused by inhomogeneities in the ionospheric electron density that existed at different spatial scales.

4.3. TEC Gradients and Plasma Bubble Identification

Ionospheric equatorial plasma bubbles (EPBs) are inhomogeneities elongated in the meridional and altitudinal directions, containing plasma with electron density much lower than the surrounding ionosphere. Large EPBs [30,31] may have complex internal structures with regions of higher and lower electron density.

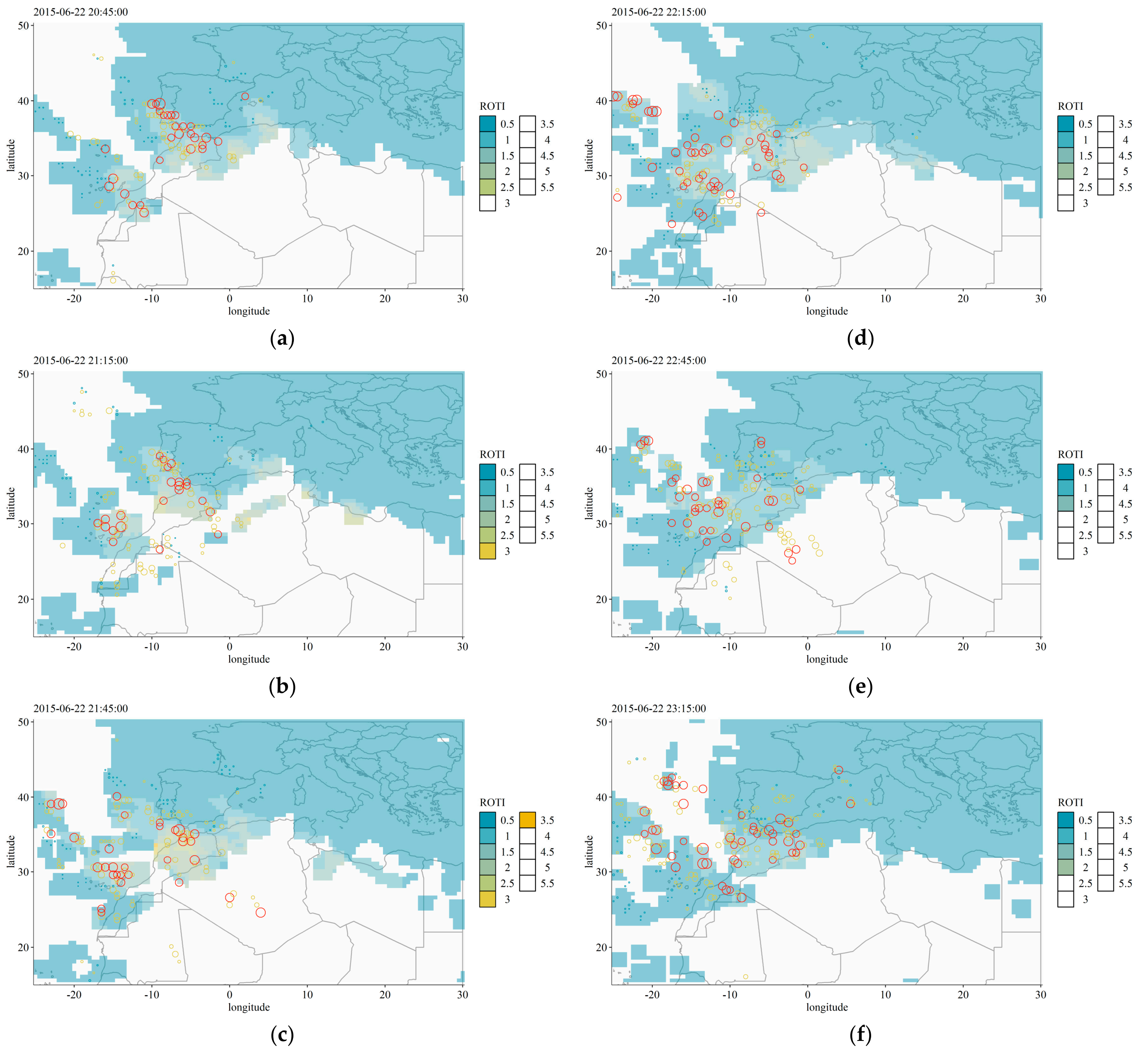

(**a**) (**d**)

(**b**) (**e**)

(**c**) (**f**)

Figure 6. ROTI maps (colours) and ROTI data from the ground-based receivers (coloured open circles; see Figure 5 for the colour scheme; size is proportional to the ROTI values) on 22 June between 20:45 and 23:30 (top to down, left to right, please see the time stamps).

EPBs were previously reported as the main sources of the ionospheric scintillations observed in the studied region during the night of 22–23 June [1,12]. To identify these structures, we used TEC spatial gradients calculated using TEC maps provided by the DRAWING-TEC project. Spatial (E–W and N–S) gradients of TEC and their variability have been demonstrated to be very effective in proxying the related scintillation on GNSS signals due to EPBs [32]. The maps of the absolute TEC gradients are shown in Figures 8 and S9 and 9 and S10 for the selected time intervals on 22 and 23 June with overplotted ROTI and S4 data, respectively. Animations containing similar plots for other time intervals, as well as the data for the longitudinal (∇xTEC) and latitudinal (∇yTEC) gradients, can be found in the Supplementary Materials (absolute gradients and ROTI: Animation S5; longitudinal gradients and ROTI: Animation S6; latitudinal gradients and ROTI: Animation

S7; absolute gradients and S4: Animation S8; longitudinal gradients and S4: Animation S9; and latitudinal gradients and S4: Animation S10).

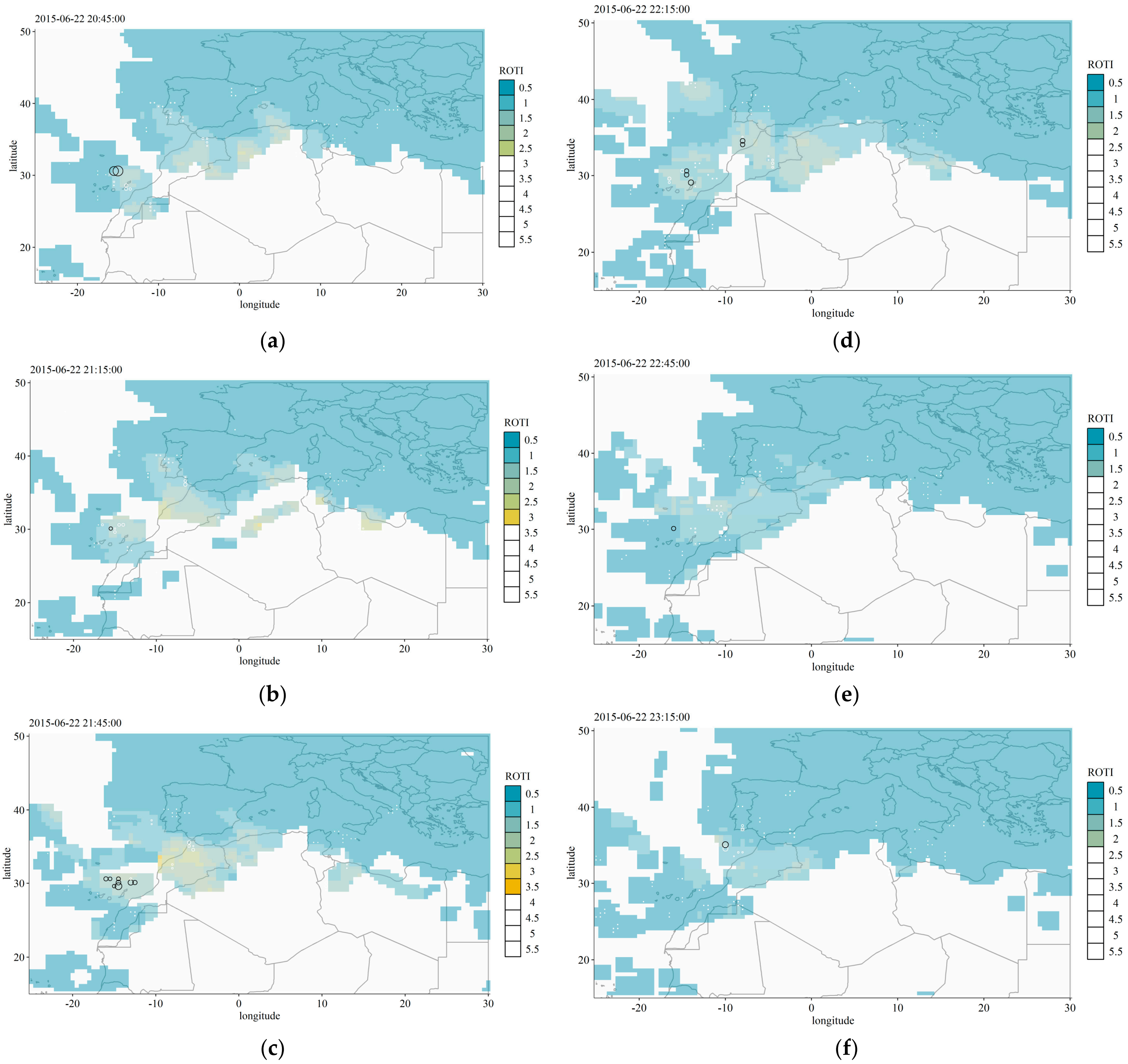

(**a**) (**d**) (**b**) (**e**) (**c**) (**f**)

Figure 7. ROTI maps (colour) and S4 measurements (open circles: white for S4 < 0.8 and black for S4 $\geq$ 0.8; size is proportional to S4 values) on 22 June between 20:45 and 23:30 (top to down, left to right, please see the time stamps).

As one can see, the areas of high ROTI and S4 values coincide with regions of high spatial TEC gradients (Figures 8–12). Spatiotemporal patterns of the variations in the scintillation indices and TEC gradients are very well correlated. These patterns include, for example, several structures stretched along the northwest–southeast direction that are seen both in the maps of the spatial gradients and the ROTI and are located between the Canary Islands/Madeira and the Iberian Peninsula. Such structures are not clearly visible in Figures 6 and 7, which show S4 values at corresponding IPPs. However, when the S4 values are overplotted on the TEC gradient maps, it is seen that most of the IPPs of the signals with high S4 values are located inside these structures. While these elongated structures were previously reported for the ROTI [1,12], in this work, by comparing the data for the spatial gradients and the ROTI and S4 data, we can conclude that the high TEC gradients depict boundaries of inhomogeneities in the ionospheric electron density that caused ionospheric scintillations.

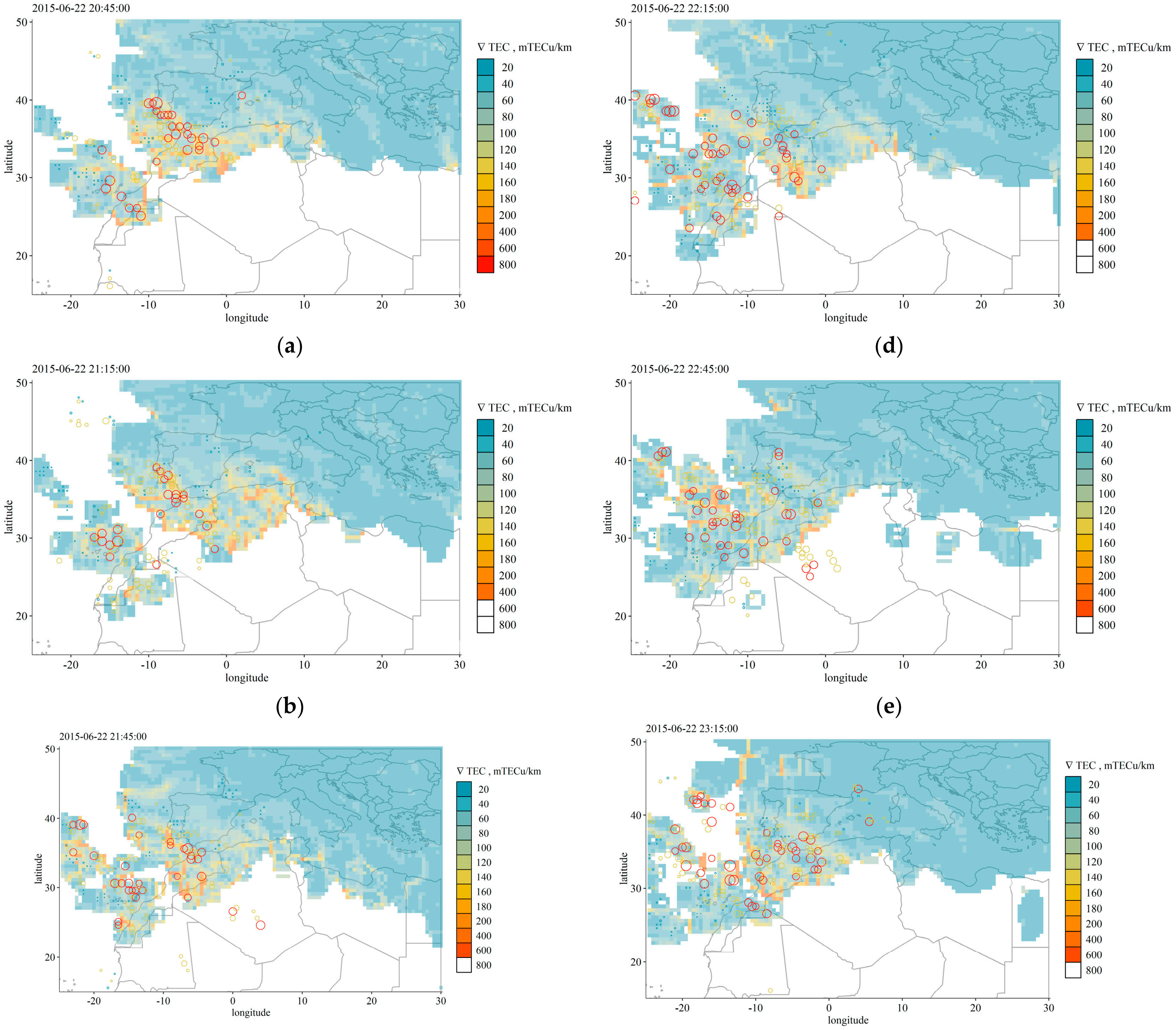

(**a**) (**d**)

(**b**) (**e**)

(**c**) (**f**)

Figure 8. Absolute TEC gradients (colour) calculated at 15-min time intervals on 22 June between 20:45 and 23:30. ROTI data from receivers are shown as open circles (coloured open circles; see Figure 5 for the colour scheme; size is proportional to the ROTI values) (please see the time stamps).

Such relations between the scintillations and the spatial gradients were already shown, for example, in the climatological analysis for the Brazilian region [32]. In this work we confirm this relation for a different region and for an individual scintillation event. Also, we can confirm another result of [32]: in general, the latitudinal (∇yTEC) TEC gradients are higher than the longitudinal (∇xTEC) ones, and, consequently, the contribution of the latitudinal gradients to the values of the absolute TEC gradients is also larger in general.

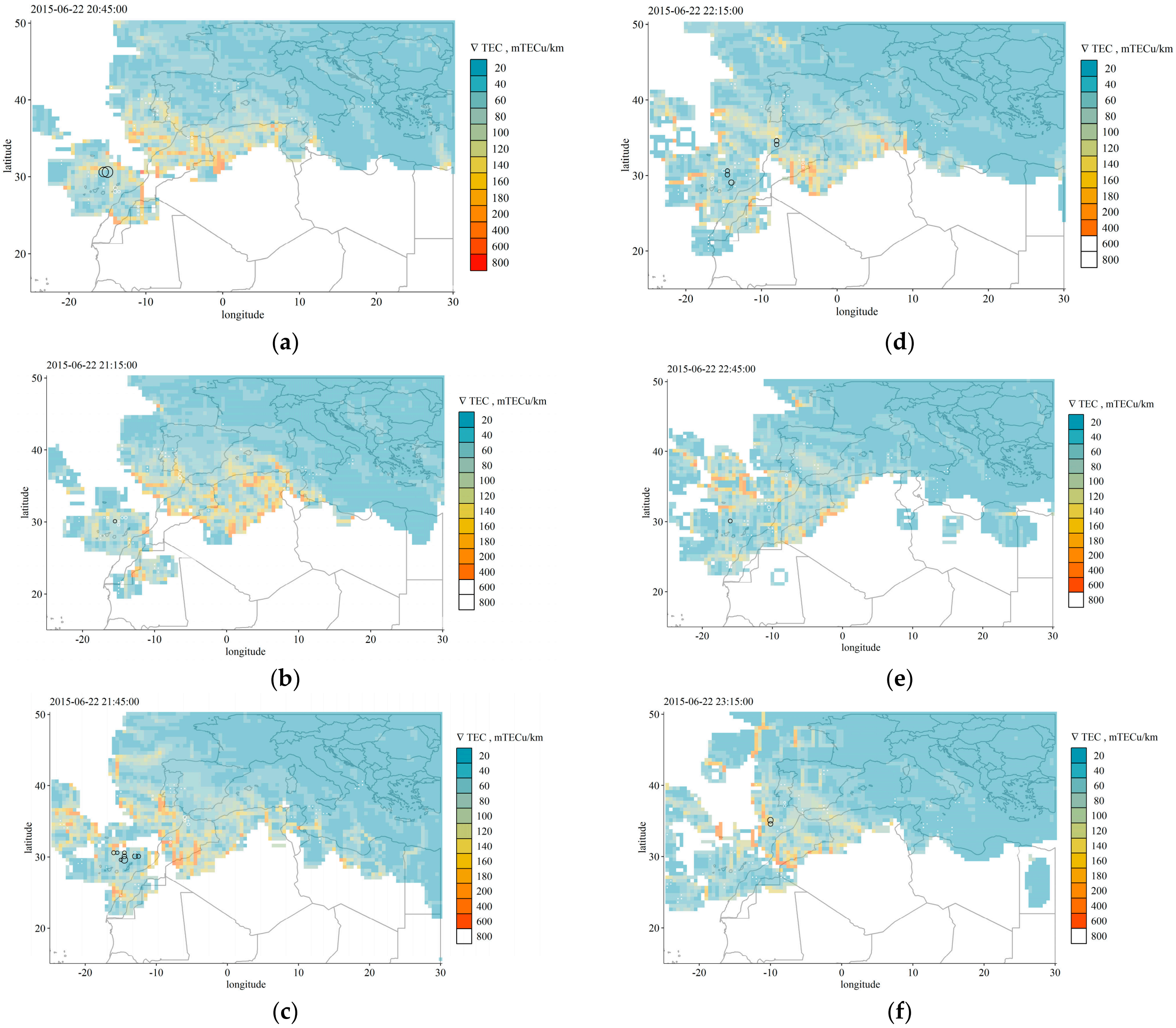

(**a**) (**d**)

(**b**) (**e**)

(**c**) (**f**)

Figure 9. TEC gradients (colour) calculated at 15-min time intervals on 22 June between 20:45 and 23:30. S4 measurements are shown as open circles (see Figure 12 for the colour scheme; size is proportional to S4 values), (top to down, left to right, please see the time stamps).

Figures 7d and S8d show EPBs identified by the Swarm mission on 23 June 2015, 01:00 UTC (vertical lines of grey dots depict Swarm PBI = 1). They are shown again in Figure 10 together with similar plots for 22 June 2015, 23:00 UTC. The plasma bubble identified by the Swarm product at 23:00 UTC on 22 June as containing EPB (vertical lines of grey dots) coincides with areas of high absolute (see Figure 10a,b) and longitudinal (see Supplementary Materials Animations S9 and S10) TEC gradients, but not with the areas of high ROTI values on the ROTI maps (see Figure 10c). On 23 June at 01:00 UTC, the areas identified by the Swarm product as containing EPBs are located between the areas of high TEC gradients (Figure 10d,e)/high ROTI values on the ROTI maps (Figure 10d,f). One of the possible explanations for no relations between the spatial TEC gradients and EPB identified by Swarm at this time is that the structures identified by the Swarm product have a smaller size than the TEC map resolution (0.5 × 0.5°).

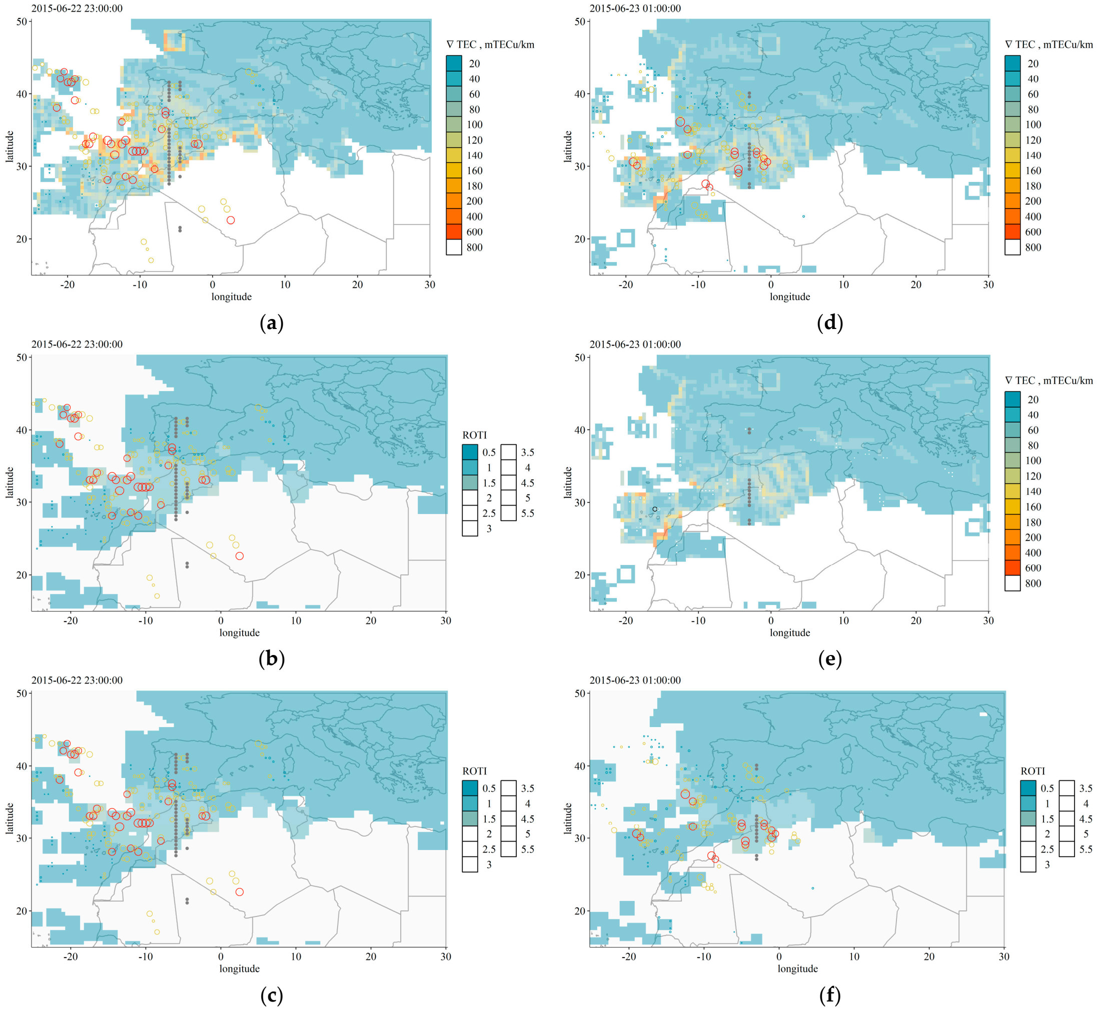

(**a**) (**d**)

(**b**) (**e**)

(**c**) (**f**)

Figure 10. Maps of the absolute TEC gradients ((**a**,**b**,**d**,**e**), colours) and ROTI ((**c**,**f**), colours) together with scintillation indices obtained from ground-based receivers: ROTI ((**a**,**c**,**d**,**f**), coloured circles; see Figure 8 for the colour scheme; size is proportional to the ROTI values) and S4 ((**b**,**e**), white and black circles; see Figure 12 for the colour scheme; size is proportional to S4 values), and the Swarm PBI detections (vertical lines of grey dots) for 22 June 23:00 and 23 June 1:00 UTC.

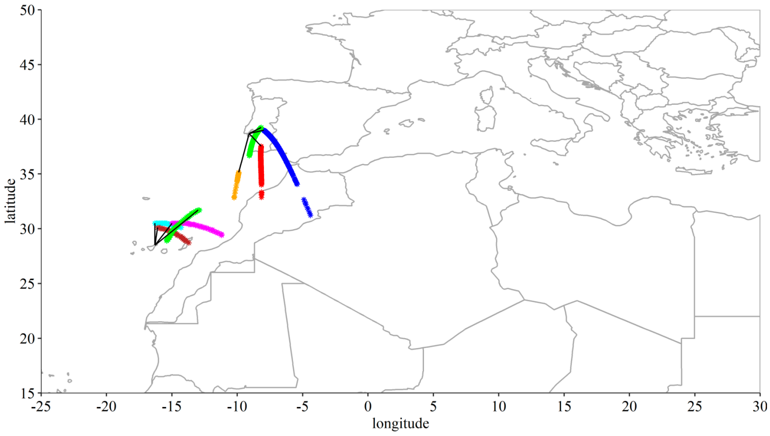

Figure 11. IPPs of several GPS satellites (see text for details)—coloured asterisks, observed at Lisbon and Tenerife during the strong scintillations (slightly different time intervals for different satellites). Black lines connect IPP trajectories to corresponding GNSS receivers and give a simplistic visualisation of corresponding LOSs.

There are other ways to confirm relations between ionospheric scintillations and depletions of the electron density, revealing the presence of EPBs, for example, by the analysis of slant TEC (sTEC) variations obtained for satellites experiencing signal scintillations [14]. To perform this analysis, we selected four satellites for both the Lisbon and Tenerife receivers, with the highest S4 values observed during the night of 22–23 June. These are satellites with PRN G09, G19, G23 and G32 for Lisbon and G01, G04, G11 and G32 for Tenerife. The sTEC values began to rise after the geomagnetic storm commencement in the late afternoon of 22 June 2015, following the positive ionospheric storm development (as described, e.g., in [7,9–11]) (corresponding plots with sTEC and S4 variations can be found in Figures S11 and S12). However, when the S4 values started to grow around 20–22 h UTC (depending on the receiver and PRN), the sTEC values dropped significantly (by 30–50 TECu as measured at Tenerife). The times of the scintillations' onsets and the sTEC decreases are well correlated for each of the satellites. According to [14], this S4-sTEC dynamics can be interpreted as an effect of a() EPB(s) crossing the line of sight (LOS) of a receiver–satellite pair. Figure 11 shows the IPPs of these satellites at the time intervals of the strongest scintillations for each of the satellites. As one can see, the directions of LOS (and locations of corresponding sTEC decreases related to EPBs) coincide very well with areas of high spatial TEC gradients (see Figures 9 and 10), allowing us to conclude that these high spatial gradients result from EPBs crossing the studied area.

4.4. GIX, NeGIX and TEGIX Indices Analysis

To cross-validate the findings of the analysis of the S4, ROTI and ∇TEC data presented above, we used the GIXy component (GNSS-based gradient ionosphere index) and NeGIX and TEGIX (Swarm data-based indices) data. Figure 12 shows half-hourly maps of the 95 percentile of the GIXy (gradient in geographic north–south direction) component from 20:30 UTC on 22 June until 2:00 UTC on 23 June. These maps clearly show clear signatures of the dynamic evolution of TEC gradients in agreement with the other aforementioned results (see Figures 9 and 12). Regions indicated by purple circles on 23 June during 00:00–2:00 UTC show the presence of positive (i.e., higher TEC for the northern IPPs) and negative (i.e., higher TEC for the southern IPPs) GIXs, indicating signatures of high dynamical regions such as IPBs. The provision of a sign in the GIX provides a unique opportunity to identify such regions. The results agree with the Swarm PBI detections (vertical lines of grey dots) in Figure 10 for 22 June 23:00 and 23 June 1:00 UTC. The GIXx (gradient in west–east direction) component does not show significant changes on gradient maps and, therefore, is not included. It must be mentioned that the observed GIX-related TEC gradients have a mid-to-large-scale character in agreement with [8]. Since S4 and ROTI data indicate small- to mid-scale irregularities, it can be concluded that the ionosphere over the south part of the Iberian Peninsula was perturbed at all spatial scales on 22 June 2015. This conclusion is confirmed by gradient estimates from Swarm data on 22 June 2015.

The NeGIX and TEGIX indices are calculated using the Swarm observations. Figures 13 (top) and 14 display the resulting electron density gradients for the orbits of Swarm A and C that navigate westwards from the evening of 22 June to the early hours of 23 June 2015. As previously, the data of only two passes of Swarm on 22 June were used for the analysis: at 21:32 UTC (along the 18°E meridian) and at 23:06 UTC (along the 5.5°W meridian). As one can see from Figure 13, these orbital passes are the ones with the strongest Ne and TEC gradients during the studied time interval. The location of these identified ionospheric perturbations in the region of the Strait of Gibraltar and Northern Africa correlates very well with other observational data presented above. As seen from Figure 14, the most extreme 95-percentile values of the electron density gradients for these two orbits are seen between 20°N and 40°N and surpassed 5000 $e/cm^3 \cdot km$ for the zonal and meridional components of NeGIX. This value is 10× greater than for the other three orbits of Swarm A and C.

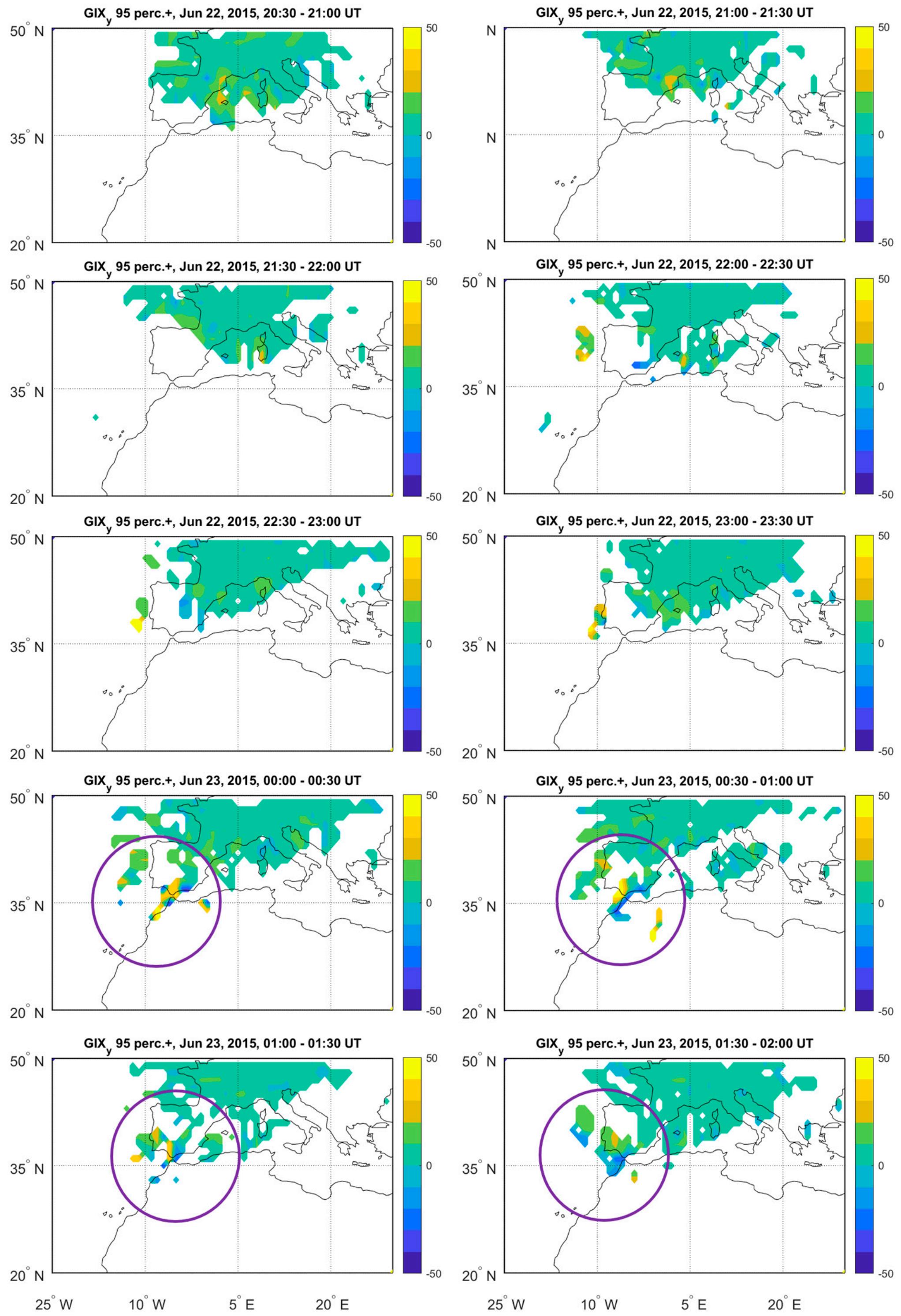

Figure 12. Maps of 95 percentile of the GIXy component (i.e., −ve means higher gradient in south–north direction) in mTECU/km averaged at every 30-min interval from 20:30 UTC on 22 June until 2:00 UTC on 23 June. The dipole length range (50–1000 km) is rather large to obtain sufficient data coverage for mapping. Regions indicated by circles show the existence of +ve and −ve gradients, indicating regions of high gradients.

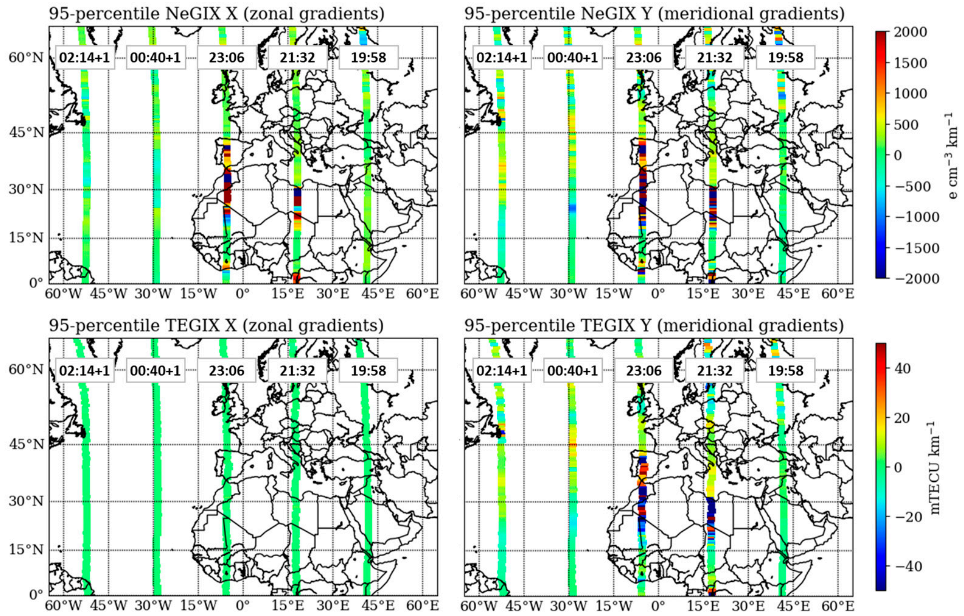

Figure 13. Resulting maps for the 95-percentile values of the X and Y components of NeGIX (**top**) and TEGIX (**bottom**). The indices are determined using data from Swarm A and C, which orbit from the right pass in the evening of 22 June towards the left in the early hours of 23 June. The paths at 21:32 and 23:06 UTC show the strongest gradients for this event and are reviewed in more detail below.

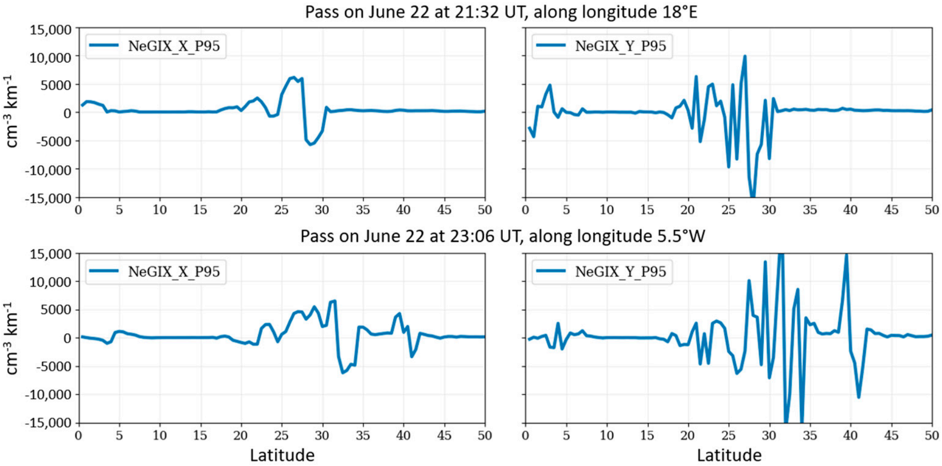

Figure 14. The 95-percentile values for the X (**left**) and Y (**right**) components of NeGIX as a function of latitude. As seen from the maps above, the two orbits of Swarm A and C with the strongest gradient values on 22 June are traced from top to bottom.

Also, the meridional component of TEGIX on the right panels of Figure 15 exposes strong 95-percentile values of TEC gradients over the same latitudinal range, reaching absolute values of more than 100 mTECU/km. For comparison, with red dashed lines, the X and Y components of the spatial gradients extracted from the ∇TEC maps (GNSS data) are overplotted as a function of latitude. The ∇TEC results are limited to latitudes above 30 N. Nevertheless, this comparative analysis with the values of TEGIX for the orbit at 21:32 UTC shows consistent results in magnitude. For the pass at 23:06 UTC, although strong TEC variability in the region is detected by the two methods, a strong difference in the amplitude of gradients is observed. This can be explained by the natural definition of these approaches. While the estimation of ∇TEC gradients is a simplified approach to comparing TEC values at adjacent grid points of TEC maps, the richer sample of Swarm A and C TEC measurements and their combination to form gradient vectors permits the deduction of a 95 percentile. In this context, Swarm permits the overcoming of limitations of data availability and resolution, as generally experienced with ∇TEC maps and ground-based GNSS techniques, especially in the studied region.

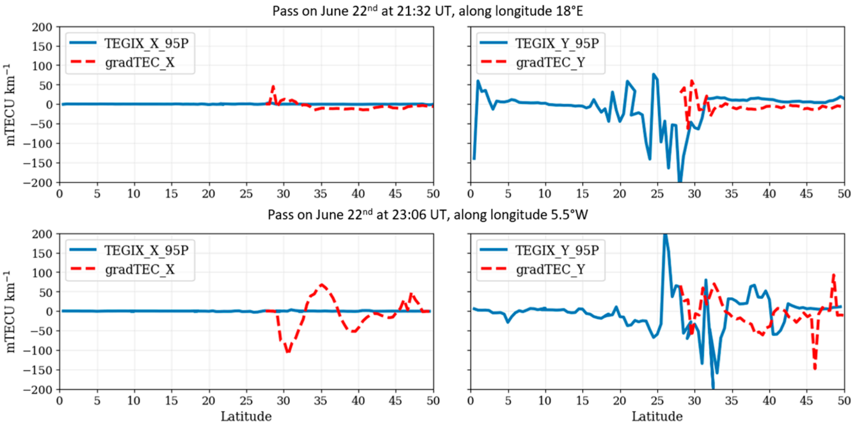

Figure 15. Comparison between the 95-percentile values for the X and Y components of TEGIX (blue lines) and the spatial gradients for similar meridians extracted from ∇TEC maps (red dashed lines) as a function of latitude. The two orbits of Swarm A and C with the strongest gradient values are displayed at 21:32 UTC (**top**) and 23:06 UTC (**bottom**).

Still, the contrast between ground-based and space-borne instruments serves to confirm the location of ionospheric inhomogeneities and the dynamics of the studied parameters.

5. Discussion and Conclusions

Monitoring ionospheric irregularities over the Western Mediterranean is of paramount importance due to the potential for small-scale irregularities to spill over into mid-latitudes, especially during disturbed geospace conditions. In the case event of the June 2015 storm, we contributed to the understanding of the conditions that lead to the penetration into these latitudes and pinpoint how their monitoring and characterisation are crucial, given the growing reliance on GNSS services and technologies, which are highly susceptible to disruptions caused by those kinds of threatening ionospheric irregularities. In fact, the continuous monitoring and analysis of ionospheric irregularities in this region (which is located in the south and southwest parts of the area covered by EGNOS, a satellite-based augmentation system developed by the European Space Agency and EUROCONTROL to enhance the reliability and accuracy of the positioning data) are essential to mitigate these risks and ensure the integrity of critical GNSS-dependent technologies.

The dynamics of the ionosphere in the low–middle latitudes of the Euro–African meridional sector during the geomagnetic storm of 22–23 June 2015 was different from what is normally expected for this region. Large variations in scintillation indices (S4 and ROTI) as well as large spatial TEC gradients were observed there between 19 h UTC on 22 June and 3 h UTC on 23 June. These ionospheric disturbances were caused by a rare event of a spill-over of EPBs from low latitudes triggered by the storm dynamics. Our finding using, for the first time, ground-based measurements of S4 amplitude scintillation indices are in agreement with previous analyses based solely on ROTI and TEC measurements (e.g., [8,11,12,14]). On the other hand, our study allowed us to access the dynamics of the ionospheric inhomogeneities on different spatial scales by comparing ROTI and S4 data and by comparing scintillation indices' variations with changes in the spatial TEC gradients. During the studied event, EPBs were seen as elongated (NW–SE) areas of lower electron density (lower TEC) travelling northwestward through the studied region. High values of S4 and ROTI obtained from individual GNSS receivers were located, as a rule, inside those areas. The spatial and temporal variations in different parameters, such as scintillation indices, TEC gradients and TEC and electron density indices, obtained from the ground-based and space-borne instruments, are consistent and clearly show that spill-over EPBs are responsible for specific ionospheric conditions that were observed during this storm in this meridional sector.

The unusual character of the ionospheric response to the storm of June 2015 was already noted in [8] when compared to the geomagnetic storm of March 2015. During the storm of March 2015, the strength of the ionospheric disturbance (measured by the GIX and SIDX indices and ROTI) gradually decreased from high (60–75°N) to low–middle (30–45°N) latitudes. This observation indicates a growing dissipation of travelling ionospheric disturbances generated by the solar energy input at high latitudes during the storm and subsequently moving equatorward. On the contrary, as is shown in [8], the highest values of the GIX were observed both at high and low–middle latitudes, and even the ROTI values obtained for the low–middle latitudes were higher than for the middle (45–60°N) latitudes. The results of a study presented in this paper allow assuming that the difference in the latitudinal response of the ionosphere to these two storms of 2015 results from the EPB spill-over event. The rapid changes in spatial gradients and positioning errors shown in [8] can also be explained by the effect of passing spilled-over EPBs. It is interesting to note that the GIX indicates medium- to large-scale (here 50–500 km) perturbations of TEC. Thus, a broad spectrum of spatial and temporal scales has been observed in the Western Mediterranean area on 22 June 2015. The related physical processes probably originate in lower latitudes.

In conclusion, this work contributes to a deeper understanding of the longitudinal variations in the North African sector, particularly in the western region, where EPB occurrences are more intense. These variations, whose origin is not completely understood, play a key role in determining the severity and frequency of EPB spill-overs, and their study is willing to contribute to future more accurate forecasting and mitigation strategies. Lastly, this work can be of support towards the planning of enhanced monitoring infrastructure and research efforts in the Western Mediterranean to address the challenges posed by ionospheric irregularities and ensure the continued reliability of GNSS services in the region.

Supplementary Materials: The following supporting information can be downloaded at: https://www.mdpi.com/article/10.3390/rs17030535/s1, Figures S1 and S2: S4 multipath analysis for Lampedusa and Tenerife, respectively (same as Figure 2); Figures S3 and S4: Time variations and azimuth–elevation distribution of S4, respectively, at Lisbon (a), Tenerife (b) and Lampedusa (c), S03: Vertical lines mark the midnight, horizontal lines mark S4 = 0.5, time is in UTC, S04: The horizontal lines mark S4 = 0.5; Figures S5 and S6: Same as Figures 4 and 5, respectively, but for 23 June between 00:15 and 1:45; Figures S7, S8, S9 and S10: Same as Figures 6–9, respectively, but for June 23 between 00:15 and 1:45. Swarm ionospheric plasma bubble index data are shown as grey dots along meridians in (d); Figure S11: S4 (a,c,e,g) and sTEC (b,d,f,h) values obtained at Lisbon for PRNs G09 (a,b), G19 (c,d), G23 (e,f) and G32 (g,h) between 18:00 UTC and 6:00 UTC of the following day for 21–23 June 2015. Colours: 21 June—black, 22 June—red, 23 June—blue, Figure S12: Same as S11 but for Tenerife and PRNs G01 (a,b), G04 (c,d), G11 (e,f) and G32 (g,h). Animation S1: Timelapse of S4 IPP maps between June 22 19:30 and June 23 02:30; Animation S2: Timelapse of ROTI IPP maps between June 22 19:30 and June 23 02:30; Animation S3: Timelapse of ROTI maps between June 22 19:30 and June 23 02:30; Animation S4: Timelapse of ROTI and S4 IPP maps between 22 June 19:30 and 23 June 2:30; Animations S5–S7: Timelapse of absolute, x and y, respectively, TEC gradient maps and ROTI between 22 June 19:30 and 23 June 2:30; Animations S8–S10: Timelapse of absolute, x and y, respectively, TEC gradient maps and S4 between 22 June 19:30 and 23 June 02:30.

Author Contributions: This work has the following contributions: conceptualization—A.M.; methodology—A.M., L.S. and T.B.; software—A.M., R.I., E.P. and D.E.; validation—A.M., L.S. and

T.B.; formal analysis—A.M.; investigation—A.M., L.S., T.B., R.I., E.P., M.M.H., J.A.C. and D.E.; resources—A.M., T.B. and L.S.; data curation—A.M., R.I. and E.P.; writing—original draft preparation—A.M.; writing—review and editing—A.M., L.S., T.B., R.I., E.P., M.M.H., J.A.C. and N.J.; visualization—A.M., J.A.C. and M.M.H.; supervision—A.M.; project administration—A.M.; funding acquisition—A.M. and L.S. All authors have read and agreed to the published version of the manuscript.

Funding: IA is supported by Fundação para a Ciência e a Tecnologia (FCT, Portugal) through the research grants UIDB/04434/2020 (https://doi.org/10.54499/UIDB/04434/2020), UIDP/04434/2020 (https://doi.org/10.54499/UIDP/04434/2020) and UID/04434/2025 . This study is a contribution to the "PROSE: P3-SWE-XXXVII—SWE PRODUCTS FOR SOUTHERN EUROPE—PHASE 1" project funded by ESA. The work was supported through the "ALERT: Assessment of the ionospheric scintillation over Portugal" project as a part of the 3rd PITHIA-NRF TNA. The PITHIA-NRF project has received funding from European Union's Horizon 2020 research and innovation program under grant agreement no. 101007599. A.M. acknowledges the research infrastructure and the access provider INGV of the PITHIA-NRF project (https://www.pithia-nrf.eu/). RI's current research fellowship is funded by the Swarm Space Weather Variability, Irregularities, and Predictive Capabilities for the Dynamic Ionosphere (Swarm-VIP-Dynamic) project, which has been funded by the European Space Agency, contract 4000143413/23/I-EB within the "Esa Solid Magnetic Science Cluster—Research Opportunities: 4dionosphere—Expro+".

Data Availability Statement: The SCINDA data are available: for [21] at Barlyaeva, T.; Barata, T.; Morozova, A. Data from: Datasets of ionospheric parameters provided by SCINDA GNSS receiver from Lisbon airport area. Mendeley Data 2020, V1. http://dx.doi.org/10.22632/kkytn5d8yc.1, accessed on 12 December 2024; for [22] at Morozova, A.; Barlyaeva, T.; Barata, T. Data from: Datasets of ionospheric parameters (TEC, SI, positioning errors) from Lisbon airport area for 2014–2019. Mendeley Data 2022, V2. http://dx.doi.org/10.22632/3z6mjk39jv.2, accessed on 12 December 2024. The RENEP RINEX 2.11 files are available through https://renep.dgterritorio.gov.pt/ (accessed on 18 November 2024). Rinex data from the mas1, lpal, rabt and meli receiver are accessible through the FTP repository of the BKG's GNSS Data Center (https://igs.bkg.bund.de/), part of the International GNSS Service (IGS). Data for the Novatel ISMR receiver operating in Lampedusa (code "lam0s") are accessible through the eSWua repository (https://doi.org/10.13127/eswua/gnss, accessed on 12 December 2024). The GNSS data for the Tenerife station are by courtesy of the Ionosphere Monitoring and Prediction Center at DLR, Germany (https://impc.dlr.de/). TEC and ROTI maps are from the DRAWING-TEC project by ISEE (https://aer-nc-web.nict.go.jp/GPS/DRAWING-TEC/), accessed on 12 December 2024 and available at https://stdb2.isee.nagoya-u.ac.jp/GPS/GPS-TEC/, accessed on 12 December 2024 and https://stdb2.isee.nagoya-u.ac.jp/GPS/GPS-TEC/GLOBAL/RMAP/index.html, accessed on 12 December 2024. Global GNSS-TEC data processing has been supported by JSPS KAKENHI Grant Number 16H06286. GNSS RINEX files for the GNSS-TEC processing are provided from many organizations listed by the webpage. (http://stdb2.isee.nagoya-u.ac.jp/GPS/GPS-TEC/gnss_provider_list.html, accessed on 12 December 2024). Ionospheric plasma bubble index is from the SW_IBIxTMS_2F Swarm product (please visit https://swarmhandbook.earth.esa.int/catalogue/sw_ibixtms_2f, accessed on 12 December 2024 for description) and available at ftp://swarm-diss.eo.esa.int/Level2daily/Latest_baselines/IBI/TMS, accessed on 12 December 2024.

Acknowledgments: Authors are grateful to Martin Kriegel (DLR) for providing Tenerife data. The authors would like to acknowledge the Direção Geral do Território (DGT) and Helena Ribeiro personally for making ReNEP data available (RENEP). The authors thank Giorgio di Sarra, Scientific director of the activities at the ENEA Climate Observation Station, and Damiano Sferlazzo for their support with the ISMR station in Lampedusa.

Conflicts of Interest: The authors declare no conflicts of interest. The funders had no role in the design of this study; in the collection, analyses, or interpretation of the data; in the writing of the manuscript; or in the decision to publish the results.

References

1. Cherniak, I.; Zakharenkova, I. First observations of super plasma bubbles in Europe. *Geophys. Res. Lett.* **2016**, *43*, 11–137. [CrossRef]
2. Pica, E.; Spogli, L.; Cesaroni, C.; Alfonsi, L.; Haralambous, H.; Vallianatos, F.; De Franceschi, G.; Romano, V.; Marcocci, C. Assessing the ionospheric scintillations occurrence on L-band in the southern Mediterranean sector. *Adv. Space Res.* **2024**, *75*, 837–855. [CrossRef]
3. Wei, Y.; Zhao, B.; Li, G.; Wan, W. Electric field penetration into Earth's ionosphere: A brief review for 2000–2013. *Sci. Bull.* **2015**, *60*, 748–761. [CrossRef]
4. Li, G.; Ning, B.; Otsuka, Y.; Abdu, M.A.; Abadi, P.; Liu, Z.; Spogli, L.; Wan, W. Challenges to equatorial plasma bubble and ionospheric scintillation short-term forecasting and future aspects in east and southeast Asia. *Surv. Geophys.* **2021**, *42*, 201–238. [CrossRef]
5. Spogli, L.; Alberti, T.; Bagiacchi, P.; Cafarella, L.; Cesaroni, C.; Cianchini, G.; Coco, I.; Di Mauro, D.; Ghidoni, R.; Giannattasio, F.; et al. The effects of the May 2024 Mother's Day superstorm over the Mediterranean sector: From data to public communication. *Ann. Geophys.* **2024**, *67*, PA218. [CrossRef]
6. Rodrigues, F.S.; Socola, J.G.; Moraes, A.O.; Martinis, C.; Hickey, D.A. On the properties of and ionospheric conditions associated with a mid-latitude scintillation event observed over southern United States. *Space Weather* **2021**, *19*, 2021SW002744. [CrossRef]
7. Morozova, A.L.; Barlyaeva, T.V.; Barata, T. Variations of TEC over Iberian Peninsula in 2015 due to geomagnetic storms and solar flares. *Space Weather* **2020**, *18*, 2020SW002516. [CrossRef]
8. Nykiel, G.; Cahuasquí, J.A.; Hoque, M.M.; Jakowski, N. Relationship between GIX, SIDX, and ROTI ionospheric indices and GNSS precise positioning results under geomagnetic storms. *GPS Solut.* **2024**, *28*, 69. [CrossRef]
9. Barata, T.; Pereira, J.; Hernández-Pajares, M.; Barlyaeva, T.; Morozova, A. Ionosphere over Eastern North Atlantic Midlatitudinal Zone during Geomagnetic Storms. *Atmosphere* **2023**, *14*, 949. [CrossRef]
10. Astafyeva, E.; Zakharenkova, I.; Alken, P. Prompt penetration electric fields and the extreme topside ionospheric response to the June 22–23, 2015 geomagnetic storm as seen by the Swarm constellation. *Earth Planets Space* **2016**, *68*, 152. [CrossRef]
11. Ngwira, C.M.; Habarulema, J.B.; Astafyeva, E.; Yizengaw, E.; Jonah, O.F.; Crowley, G.; Gisler, A.; Coffey, V. Dynamic response of ionospheric plasma density to the geomagnetic storm of 22–23 June 2015. *J. Geophys. Res. Space Phys.* **2019**, *124*, 7123–7139. [CrossRef]
12. Cherniak, I.; Zakharenkova, I.; Sokolovsky, S. Multi-instrumental observation of storm-induced ionospheric plasma bubbles at equatorial and middle latitudes. *J. Geophys. Res. Space Phys.* **2019**, *124*, 1491–1508. [CrossRef]
13. Pi, X.; Mannucci, A.J.; Lindqwister, U.J.; Ho, C.M. Monitoring of global ionospheric irregularities using the worldwide GPS network. *Geophys. Res. Lett.* **1997**, *24*, 2283–2286. [CrossRef]
14. Kashcheyev, A.; Migoya-Orué, Y.; Amory-Mazaudier, C.; Fleury, R.; Nava, B.; Alazo-Cuartas, K.; Radicella, S.M. Multivariable comprehensive analysis of two great geomagnetic storms of 2015. *J. Geophys. Res. Space Phys.* **2018**, *123*, 5000–5018. [CrossRef]
15. Yeh, K.C.; Liu, C.H. Radio wave scintillations in the ionosphere. *Proc. IEEE* **1982**, *70*, 324–360. [CrossRef]
16. Fremouw, E.J.; Leadabrand, R.L.; Livingston, R.C.; Cousins, M.D.; Rino, C.L.; Fair, B.C.; Long, R.A. Early results from the DNA Wideband satellite experiment—Complex-signal scintillation. *Radio Sci.* **1978**, *13*, 167–187. [CrossRef]
17. Bougard, B.; Sleewaegen, J.M.; Spogli, L.; Veettil, S.V.; Monico, J.F. CIGALA: Challenging the solar maximum in Brazil with PolaRxS. In Proceedings of the 24th International Technical Meeting of the Satellite Division of the Institute of Navigation (Ion GNSS 2011), Portland, OR, USA, 20–23 September 2011; pp. 2572–2579.
18. Van Dierendonck, A.J.; Klobuchar, J.; Hua, Q. Ionospheric scintillation monitoring using commercial single frequency C/A code receivers. *Proc. ION GPS* **1993**, *93*, 1333–1342.
19. Mrak, S.; Coster, A.J.; Groves, K.; Nikoukar, R. Ground-based infrastructure for monitoring and characterizing intermediate-scale ionospheric irregularities at mid-latitudes. *Front. Astron. Space Sci.* **2023**, *10*, 1091340. [CrossRef]
20. Wernik, A.W.; Secan, J.A.; Fremouw, E.J. Ionospheric irregularities and scintillation. *Adv. Space Res.* **2003**, *31*, 971–981. [CrossRef]
21. Barlyaeva, T.; Barata, T.; Morozova, A. Datasets of ionospheric parameters provided by SCINDA GNSS receiver from Lisbon airport area. *Data Brief* **2020**, *31*, 105966. [CrossRef]
22. Morozova, A.; Barlyaeva, T.; Barata, T. Updating datasets of ionospheric parameters provided by SCINDA GNSS receiver from Lisbon airport area with full data sets for 2014–2019. *Data Brief* **2023**, *47*, 109026. [CrossRef] [PubMed]
23. Morozova, A. Ionosphere scintillations. In *Space Weather Influence on the Ionosphere and Its Potential Threats to GNSS Services: Focus on the Portuguese Territories*; Morozova, A., Barlyaeva, T., Eds.; Materials of the on-line workshop "Space weather influence on the ionosphere and its potential threats to GNSS services: Focus on the Portuguese territories"; Instituto de Astrofísica e Ciências do Espaço: Lisbon, Portugal, 2023; ISBN 978-989-33-5493-3/978-989-33-5492-6. [CrossRef]
24. Cesaroni, C.; De Franceschi, G.; Marcocci, C.; Pica, E.; Romano, V.; Spogli, L. *Electronic Space Weather Upper Atmosphere Database (eSWua)—GNSS Scintillation Data*; Version 1.0.; Upper atmosphere physics and radiopropagation Working Group, Istituto Nazionale di Geofisica e Vulcanologia: Roma, Italy, 2020. [CrossRef]

25. Jakowski, N.; Hoque, M.M. Estimation of spatial gradients and temporal variations of the total electron content using ground-based GNSS measurements. *Space Weather* **2019**, *22*, 339–356. [CrossRef]
26. Cahuasquí, J.A.; Hoque, M.M.; Jakowski, N.; Vasylyev, D.; Buchert, S.; Nykiel, G.; Kriegel, M.; David, P.; Tagargouste, Y.; Berdermann, J. NeGIX and TEGIX: Two new indices to characterize the topside ionosphere with Swarm (No. EGU24-12608). *Copernic. Meet.* **2024**. [CrossRef]
27. McCaffrey, A.M.; Jayachandran, P.T. Spectral characteristics of auroral region scintillation using 100 Hz sampling. *GPS Solut.* **2022**, *21*, 1883–1894. [CrossRef]
28. Imam, R.; Alfonsi, L.; Spogli, L.; Cesaroni, C.; Mehr, I.E.; Minetto, A.; Dovis, F. Scintillation Climatology from a Software Defined Radio Receiver over Antarctica. *Ann. Geophys.* **2024**, *67*, PA108. [CrossRef]
29. Liu, Q.; Hernández-Pajares, M.; Yang, H.; Monte-Moreno, E.; García-Rigo, A.; Lyu, H.; Olivares-Pulido, G.; Orús-Pérez, R. A New Way of Estimating the Spatial and Temporal Components of the Vertical Total Electron Content Gradient Based on UPC-IonSAT Global Ionosphere Maps. *Space Weather* **2022**, *20*, e2021SW002926. [CrossRef]
30. Yokoyama, T. A review on the numerical simulation of equatorial plasma bubbles toward scintillation evaluation and forecasting. *Prog. Earth Planet. Sci.* **2022**, *4*, 37. [CrossRef]
31. Rino, C.; Yokoyama, T.; Carrano, C. A three-dimensional stochastic structure model derived from high-resolution isolated equatorial plasma bubble simulations. *Earth Planets Space* **2023**, *75*, 64. [CrossRef]
32. Cesaroni, C.; Spogli, L.; Alfonsi, L.; De Franceschi, G.; Ciraolo, L.; Monico, J.F.G.; Scotto, C.; Romano, V.; Aquino, M.; Bougard, B. L-band scintillations and calibrated total electron content gradients over Brazil during the last solar maximum. *J. Space Weather. Space Clim.* **2015**, *5*, A36. [CrossRef]